Structural Analysis of a Nitrogenase Iron Protein from *Methanosarcina*acetivorans: Implications for CO₂ Capture by a Surface-Exposed [Fe₄S₄]

Cluster

Lee A. Rettberg,^{a†} Wonchull Kang,^{a†} Martin T. Stiebritz,^{a†} Caleb J. Hiller,^{a,b} Chi Chung Lee,^a Jasper Liedtke,^a Markus W. Ribbe,^{a,b*} Yilin Hu^{a*}

^aDepartment of Molecular Biology and Biochemistry, University of California, Irvine, CA 92697-3900; ^bDepartment of Chemistry, University of California, Irvine, California 92697-2025

[†]These authors contributed equally to this work.

*Correspondence should be addressed to yilinh@uci.edu or mribbe@uci.edu.

Running Title: Structural implications for CO₂ Capture by a Nitrogenase Iron Protein from *Methanosarcina acetivorans*

Keywords: Methanogen | Nitrogenase | Iron Protein | FeS Cluster | CO₂ Capture

ABSTRACT

Nitrogenase iron (Fe) proteins reduce CO₂ to CO and/or hydrocarbons under ambient conditions. Here, we report a 2.4 Å crystal structure of the Fe protein from *Methanosarcina acetivorans* (*Ma*NifH) that is generated in the presence of a reductant, dithionite, and an alternative CO₂ source, bicarbonate. Structural analysis of this methanogen Fe protein species suggests that CO₂ is possibly captured in an unactivated, linear conformation near the [Fe₄S₄] cluster of *Ma*NifH by a conserved arginine (Arg) pair in a concerted and, possibly, an asymmetric manner. Density functional theory calculations and mutational analyses provide further support for the capture of CO₂ on *Ma*NifH while suggesting a possible role of Arg in the initial coordination of CO₂ via hydrogen bonding and electrostatic interactions. These results provide a useful framework for further mechanistic investigations of CO₂ activation by a surface-exposed [Fe₄S₄] cluster, which may facilitate future development of FeS catalysts for ambient conversion of CO₂ into valuable chemical commodities.

IMPORTANCE

This work reports the crystal structure of a previously uncharacterized Fe protein from a methanogenic organism, which provides important insights into the structural properties of the less characterized, yet highly interesting archaeal nitrogenase enzymes. Moreover, the structure-derived implications for CO₂ capture by a surface-exposed [Fe₄S₄] cluster point to the possibility of developing novel strategies for CO₂ sequestration while providing the initial insights into the unique mechanism of FeS-based CO₂ activation.

INTRODUCTION

Iron-sulfur (FeS) proteins utilize a wide array of FeS clusters to play key roles that range from electron transfer and catalysis to structural and regulatory functions in biological systems (1-7). A homodimer carrying a subunit-bridging [Fe₄S₄] cluster at the protein surface, the iron (Fe) protein of nitrogenase is best known for its function as an obligate electron donor for its catalytic partner during substrate turnover (8, 9). Recently, the Fe protein from a diazotrophic microbe, Azotobacter vinelandii (designated AvNifH) was shown to act as a reductase on its own and catalyze the ambient reduction of CO₂ to CO via redox changes of its [Fe₄S₄] cluster (10). Interestingly, while the cluster of AvNifH is believed to cycle between the $[Fe_4S_4]^{1+}$ (reduced) and $[Fe_4S_4]^{2+}$ (oxidized) states (11-15) for its function as an electron donor in nitrogenase catalysis, catalytic turnover of CO₂ by AvNifH on its own was observed when a strong reductant, europium(II) diethylenetriaminepentaacetic acid (Eu^{II}-DTPA; E^{0} := -1.14 V at pH 8.0), poised its cluster in the all-ferrous, [Fe₄S₄]⁰ state under in vitro conditions (10). Perhaps more interestingly, the Fe protein from a methanogenic microorganism, Methanosarcina acetivorans (designated MaNifH), was capable of reducing CO₂ past CO into hydrocarbons under ambient conditions in the presence of Eu^{II}-DTPA, further illustrating the unique reactivity of the [Fe₄S₄] cluster toward CO₂ (16, 17). Together, these observations point to the nitrogenase Fe protein as a simple model system for mechanistic investigations of FeS-based CO₂ activation and reduction.

Of the two Fe protein species that have been investigated for their reactivity toward CO₂, MaNifH is particularly interesting given its ability to convert CO₂ to CO and hydrocarbons. Despite its archaeal origin, MaNifH shares a sequence identity of 59% and a sequence homology of 72% with AvNifH. Like AvNifH, MaNifH is a homodimer of ~60 kDa, and it contains a [Fe₄S₄] cluster that can adopt three oxidation states upon redox treatments: (i) the oxidized state ([Fe₄S₄]²⁺),

which is generated upon treatment by indigodisulfonate; (*ii*) the reduced state ([Fe₄S₄]¹⁺), which is generated upon treatment by dithionite; and (*iii*) the 'super-reduced', all-ferrous state ([Fe₄S₄]⁰), which is generated upon treatment by Eu^{II}-DTPA (17). There are differences, however, in the electronic properties of MaNifH and AvNifH, which are reflected by a stronger S = 3/2 contribution to the EPR spectrum of the reduced MaNifH and a decreased intensity of the parallel mode, g = 16.4 signal in the EPR spectrum of the super-reduced MaNifH (17). These differences, along with the lower reduction potential of the [Fe₄S₄]^{1+/2+} pair of MaNifH ($E^0 = -395$ mV) than that of AvNifH ([Fe₄S₄]^{1+/2+}: $E^0 = -301$ mV) (16), may contribute to the difference in the reactivity of MaNifH and AvNifH toward CO₂. The redox dependence of this reaction is further illustrated by a substantially decreased CO₂-reducing activity of both MaNifH and AvNifH in the presence of dithionite, a weaker reductant than Eu^{II}-DTPA that renders the clusters of these Fe proteins in the catalytically inefficient [Fe₄S₄]¹⁺ state (10, 16).

The significantly decreased activity of Fe protein in a dithionite-driven reaction could prove advantageous for capturing CO₂ in an early stage of CO₂ reduction. Here, we report a 2.4 Å crystal structure of *Ma*NifH that is generated in the presence of dithionite and an alternative CO₂ source, bicarbonate. Structural analysis of this previously uncharacterized Fe protein from the methanogen nitrogenase family suggests that CO₂ is possibly captured in an unactivated, linear conformation on the dithionite-reduced *Ma*NifH; moreover, it reveals the initial coordination of CO₂ by a conserved, surface-exposed arginine (Arg) pair in a concerted yet asymmetric manner, which could assist in trapping CO₂ near the [Fe₄S₄] cluster via hydrogen bonding and electrostatic interactions. These results provide a useful framework for further exploration of the mechanism of CO₂ activation by Fe proteins, which may enable future development of FeS catalysts for recycling the greenhouse gas CO₂ into valuable chemical commodities.

RESULTS

Structural analysis of the dithionite-reduced MaNifH. Consistent with the presence of its [Fe₄S₄] cluster in the +1 oxidation state, MaNifH crystallized in the presence of dithionite had a characteristic brown color. The ~2.4 Å structure of the dithionite-reduced MaNifH (PDB ID: 6NZY) adopts the same overall conformation as all Fe protein structures reported to date (9, 18-20), with each of its subunits fold as a single α/β -type domain and its [Fe₄S₄] cluster situated in a surface cavity between the two subunits (Figure 1A, B). A closer examination of the region surrounding the active site of MaNifH (Figure 1C) reveals the ligation of the [Fe₄S₄] cluster by four Cys residues, two from subunit A (Cys95^A, Cys130^A) and two from subunit B (Cys95^B, Cys130^B). Interestingly, the electron density omit map (Fo-Fc) of the active site of MaNifH (Figure 1C, $green\ mesh$; $also\ see\ Figure\ S1$) indicates the presence of additional electron density that lies immediately next to the crystallographic symmetry axis, seemingly held by two pairs of conserved Arg residues (R98^A and R98^B)—one from each of the two adjacent MaNifH subunit dimers.

Modeling the extra electron density in the structure of dithionite-reduced *Ma*NifH. Given that the additional electron density may originate from the small molecules in the protein preparations or crystallographic solutions, we then considered possible candidates and modeled water (Figure S2A), carbonate (Figure S2B), glycerol (Figure S2C) and CO₂ (Figure S2D), respectively, into this density. Water is an unlikely contributor to this density, as modeling of one water molecule in the asymmetric unit and another in its symmetry mate results in substantial "leftover" electron density in the Fo-Fc omit map (Figure S2A, *green mesh*). Carbonate and glycerol, on the other hand, could be modeled as two molecules—each at ~50% occupancy—at the crystallographic symmetry axis with reasonable R-factor values (Table S1). Similarly, CO₂ could be modeled with reasonable R-factor values at the crystallographic symmetry axis; only in

this case, two molecules of CO₂—each at 100% occupancy—could be assigned to the asymmetric unit and its symmetric mate, respectively (Table S1). It should be noted that the modeling of two CO₂ moieties results in some negative electron density; however, the overall crystallographic statistics is reasonable to support this model (Table S1) despite the difficulty to conclusively assign this ligand near the crystallographic symmetry axis.

DFT calculations of the affinity of CO₂ to the dithionite-reduced MaNifH. To seek support for the assignment of CO₂ as the extra electron density in the crystal structure of MaNifH, we then used density functional theory (DFT) calculations to analyze the CO_2 affinity of the $\lceil Fe_4S_4 \rceil^{1+}$ cluster in MaNifH. Consistent with our previous findings for both AvNifH-bound and synthetic [Fe₄S₄] clusters (10, 16), CO₂ does not interact well with the [Fe₄S₄]¹⁺ cluster of MaNifH and tends to dissociate from the cluster during the course of structural optimization; however, the two highly conserved Arg residues in MaNifH (R98A, R98B) form a cage-like configuration around the CO2 molecule that assists in trapping it in close proximity to the cluster (Video S1). Interestingly, the location of the CO₂ moiety in the DFT-optimized model is in good agreement with half of the electron density pattern in the structure of MaNifH except for a slight reorientation of CO₂ (Figure 2). In comparison, DFT optimization reveals protonation of carbonate by R98^B, followed by coordination of the resulting bicarbonate in a position parallel to the upper surface of the [Fe₄S₄] cluster, which is rather distinct from the perpendicular position modeled for carbonate in the crystal structure of MaNifH (Figure S3). This observation is important, as it provides theoretical support for the assignment of CO₂ as a potential ligand in the structure of the dithionite-reduced MaNifH protein. The fact that the MaNifH crystals were generated at a bicarbonate concentration in the same order of magnitude as that used to generate a CO₂-bound conformation of CO dehydrogenase (21) provides further support for the assignment of CO₂ in the MaNifH structure. In this scenario,

the CO_2 moiety has its C atom placed at a distance of ~4 Å to the nearest Fe atom (Fe3) of the $[Fe_4S_4]$ cluster, with the NH_2^+ groups of $R98^A$ and $R98^B$ assuming the 'distal' and 'proximal' positions, respectively, to Fe3 (Figure 2). This observation suggests a possible role of the conserved Arg pair in capturing CO_2 via hydrogen bonding and/or electrostatic interactions, as well as a potentially asymmetric functionality of the two Arg residues in this process.

Examining the role of the conserved Arg pair of MaNifH in CO₂ capture. To test the proposed role of conserved Arg residues in CO₂ capture, we performed site-directed mutagenic analysis and mutated R98 of MaNifH to either a His or a Gly. Both R98H and R98G MaNifH variants display the same S = 1/2 EPR signal as the wildtype protein, which is indicative of an unperturbed [Fe₄S₄] center in the +1 oxidation state (Figure 3A). However, the R98H variant of MaNifH retains ~80% CO₂-reducing activity, whereas the R98G variant loses ~85% of this activity (Figure 3B), consistent with the preservation (*i.e.*, the R \rightarrow H mutation) or elimination (*i.e.*, the R \rightarrow G mutation) of the hydrogen bonding ability at the position of R98. The somewhat decreased activity of the R98H variant could be explained by a shorter side chain of His and, consequently, a reduced efficiency of this residue in hydrogen bonding/proton donation than Arg. The slight defect of His in proton donation would also account for a shift of the product profile of the R98H variant (hydrocarbons/CO ratio: 1.9) from hydrocarbon formation to CO formation as compared to that of the wildtype MaNifH (hydrocarbons/CO ratio: 2.7), as formation of CO requires fewer protons than that of hydrocarbons.

Proposal of a plausible mechanism for the initial capture of CO_2 by MaNifH. To obtain further insights into the mechanism of CO_2 capture by nitrogenase Fe proteins, we compared our dithionite-reduced MaNifH structure (PDB ID: 6NZY) that is potentially bound with CO_2 with a previously reported, dithionite-reduced AvNifH structure (PDB ID: 1G5P) that is free of CO_2 (19).

Consistent with a high degree of sequence homology between MaNifH and AvNifH, the subunits A and B in MaNifH show Cα-deviations of only 0.599 and 0.616 Å, respectively, relative to those in AvNifH; yet, the two subunit chains in MaNifH are more similar to each other in terms of secondary structural elements, particularly with respect to the structurally less conserved α -helical regions (Figures S4, S5). More strikingly, compared to their counterparts in AvNifH, there is a notable movement of the two subunits of MaNifH with respect to each other, which flattens the surface cavity and consequently 'pushes' the [Fe₄S₄] cluster further toward the surface where a CO₂ molecule could be modeled (Figure S6; Video S2). A top-view comparison between the two structures further reveals a 'linearization' of helices CA and CB in MaNifH relative to those in AvNifH, which is accompanied by a substantial swing of the Arg pair, R98^A and R98^B (located at the tips of helices C^A and C^B), toward the center of the surface cavity (Figure S6; Video S3). Such a movement of the conserved Arg pair could reflect a concerted action of the 'distal' R98A and the 'proximal' $R98^B$ in the initial capture of CO_2 in an unactivated, linear conformation near the Fe3 atom of the [Fe₄S₄] cluster (see Figure 4). Further activation of CO₂ into a bent, carboxylate-like conformation may continue to employ an asymmetric mechanism. Previous DFT calculations of CO₂ activation by the catalytically competent, all-ferrous AvNifH (10) led to the proposal of binding of an activated CO₂ moiety via coordination of C to Fe3 of the cluster and coordination of O to the guanidinium group of the 'proximal' R100^B (corresponding to the 'proximal' R98^B in MaNifH), with the latter potentially donating protons for the subsequent C-O bond cleavage.

DISCUSSION

In light of a plausible asymmetric mechanism of CO₂ activation by Fe protein, it is interesting to consider the mechanism proposed for the Ni-dependent CO dehydrogenase in CO₂ activation,

which involves the action of the Fe/Ni atoms of its heterometallic C-cluster ([NiFe₄S₄]) as a pair of Lewis acid/base to facilitate scission of a C-O bond (21-24). In the absence of such a heterometal-based asymmetry, it is plausible that activation of CO₂ by the homometallic [Fe₄S₄] cluster would resort to a structure-based asymmetry that enables interactions between O and the guanidinium group of the proximal Arg, as well as binding of C to the nearest Fe3 atom. It is worth noting that the proposed asymmetric functionality of the conserved Arg pair in CO₂ activation is consistent with the previously established regulatory mechanism of nitrogenase activity through ADP-ribosylation of only one of these conserved Arg residues (25); whereas the structure-based suggestion of a single reactive Fe (Fe3) site for CO₂ activation may have certain relevance to the unique Fe site that was identified by earlier Mössbauer studies of the all-ferrous Fe protein (14). While the functions of these asymmetric elements await further elucidation, the current study provides a useful framework for investigating the structural basis of Fe protein-based CO₂ capture and activation. Moreover, the strategy utilized by the Fe protein to trap CO₂ by a pair of surfacelocated arginines loosely resembles the approaches that employ nitrogen-based ligands, such as metal-organic-frameworks (MOFs) with amine or amide groups (26) or protein amyloid fibers comprising lysines in stacked sheets (27), for CO₂ capture and sequestration. The fact that the arginine residues of the Fe protein trap CO₂ in the close proximity of a surface-exposed [Fe₄S₄] cluster for further processing may provide a conceptual basis for the future development of MOFor protein-based FeS catalysts that couple the capture of CO₂ with the recycling of this greenhouse into useful chemical commodities.

MATERIALS AND METHODS

Protein Purification and Crystallization. All protein purification steps were carried out anaerobically using Schlenk techniques. His-tagged *Ma*NifH was purified by immobilized metal affinity as described elsewhere (17, 28). Reagents for protein crystallization were purchased from Hampton Research and were thoroughly de-aerated by vacuum/Ar-fill cycling before use. All crystals were generated at room temperature in an anaerobic chamber (Coy Laboratory Products), coated with Parabar 10312 oil (Hampton Research) as a cryo-protectant and flash-frozen in liquid N₂ for data collection.

MaNifH was crystallized at room temperature by microbatch method under a layer of Al's oil (Hampton Research). The purified MaNifH protein was desalted on a G-25 fine column equilibrated with buffer M (10 mM EPPS (pH 8.0), 100 mM NaCl, 10% (v/v) glycerol, and 2 mM dithionite (DT)), and then concentrated to 10 mg/mL by Amicon Ultra-4 30 kDa centrifugal filter units. The crystals were grown by evaporating a mixture of 1 μL protein solution and 3 μl precipitant solution (2.3 M ammonium sulfate, 7% (w/v) PEG 3350, 12 mM carbonate, and 2 mM DT) under Al's oil. The protein solution was brown, indicating that the protein-bound cluster was present in the reduced, +1 state. Brown crystals grew after two weeks and were flash-frozen in liquid nitrogen for data collection.

Data Collection and Structural Determination. The diffraction data of *Ma*NifH crystals were collected at 100 K on beamline 8.2.1 of Advanced Light Source using a wavelength of 0.9774 Å and an ADSC Q315r CCD detector. 501 images were recorded for *Ma*NifH at a distance of 450 mm, with an oscillation angle of 0.25° and an exposure time of 0.25 s. The raw data were indexed and processed using iMosflm and Scala in CCP4 package (29). Molecular replacement was performed with *Phaser* in PHENIX (30) using the structure of the *Clostridium pasteurianum* NifH protein (PDB ID: 1CP2) (19) as a search model. The initial model was further improved by cycles

of manual building and refinement using Coot and PHENIX (30-32). At the end of the refinement cycle, water, carbonate, glycerol or CO₂ was manually put into the model of *Ma*NifH and further refined for 3 cycles using PHENIX. The stereochemical quality of the final structures was evaluated by MolProbity (33). All molecular graphics were prepared using PyMol (34). Data collection and statistics for refinement and ligand modelling are summarized in Table S1. The structure of DT-reduced *Ma*NifH (PDB ID: 6NZY) was deposited in the Protein Data Bank (https://www.wwpdb.org) and will be released upon publication.

Strain Construction and Activity Analyses. Strains expressing R98H and R98G *Ma*NifH variants were constructed via site-directed mutagenesis of the wildtype *Methanosarcina* acetivorans nifH sequence carried on a pET14b vector (17), followed by transformation of the resultant plasmids into the *E. coli* strain BL21(DE3). The *in vitro* CO₂-reduction assays were carried out in 9.4 mL assay vials with crimped butyl rubber serum stoppers. Each assay contained, in a total volume of 1.0 mL, 500 mM Tris-HCl (pH 10.0), 0.5 mg Fe protein (wildtype, R98H or R98G *Ma*NifH), and 100 mM Eu^{II}-DTPA. In addition, the headspace of each assay contained 100% CO₂ (for reactions) or 100% Ar (for controls). The assays were assembled without protein and Eu^{II}-DTPA, repeatedly flushed and exchanged with CO₂, followed by equilibration for 30 min until pH stabilized at ~8.0. The reaction was initiated upon addition of *Ma*NifH, followed immediately by addition of Eu^{II}-DTPA and incubation with continuous shaking at 30°C for 300 min until the reaction was complete. Following the quenching of each assay by 100 μL of 30% trichloroacetic acid, the headspace sample was examined for the production of CO and hydrocarbons as described previously (16).

EPR spectroscopy analyses. The EPR samples were prepared in a Vacuum Atmospheres glove box and flash frozen in liquid N₂ prior to analysis. The DT-reduced samples contained 2

mM DT, 50 mM Tris-HCl (pH 8.0), 500 mM NaCl and 10% (v/v) glycerol. EPR spectra were recorded by an ESP 300 Ez spectrophotometer (Bruker) interfaced with an ESR-9002 liquid-helium continuous-flow cryostat (Oxford Instruments) using a microwave power of 50 mW, a gain of 5×10⁴, a modulation frequency of 100 kHz, and a modulation amplitude of 5 G. Five scans were recorded for each EPR sample at a temperature of 10 K and a microwave frequency of 9.62 GHz.

Density functional theory calculations. The mechanism of CO_2 , carbonate and bicarbonate coordination was studied with the DFT programs in the Turbomole package, version 7.0 (35). Atomistic models of the [Fe₄S₄] cluster and its immediate protein environment were generated from the structure of MaNifH (PDB ID: 6NZY; this work) in the DT-reduced, [Fe₄S₄]¹⁺ state.

The models were selected as described previously (10) and contained the [Fe₄S₄] cluster and C95^A, C95^B, C130^A, C130^B, R98^A, R98^B, F133^A, F133^B and, additionally, the main chain atoms of the residues A96^A, A96^B, A97^A, G97^B, G131^A, G131^B, G132^A and G132^B of MaNifH to account for all interactions of the cluster with the protein backbone. N-termini were saturated with acetyl groups according to the crystallographic atom positions. Hydrogen atoms were added to the model with Open Babel (36), assuming protonation of the Arg residues. During structural optimizations, the atoms of the cluster, the side-chain atoms of the cluster-coordinating Cys residues (including C α), the side-chain atoms of the Arg residues (starting from C γ), the benzene groups of the Phe residues and all hydrogen atoms were allowed to spatially relax. All other atoms were kept structurally frozen. The models were treated as openshell systems in the unrestricted Kohn-Sham framework. Solvent effects were treated implicitly by the conductor-like solvent screening model (COSMO) (37), assuming a dielectric constant of ε =40. The structures were optimized with the TPSS functional (18). A def2-TZVP basis set (39, 40) was used for the [Fe₄S₄] cluster, the side chain atoms of the Cys residues (including

Cα atoms), the atoms of the guanidinium groups and the cluster-bound CO₂, carbonate and bicarbonate moieties. A def2-SVP basis set was assigned to all remaining atoms to accelerate the calculations. Computational time was further reduced by utilizing the resolution-of-the-identity approximation (41, 42). Antiferromagnetic coupling in the FeS cluster was accounted for by the broken symmetry approach (43-45).

ACKNOWLEDGMENTS

We thank Andrew Ma and Zihao Chen for technical assistance. This work was supported by NSF CAREER grant CHE-1651398 (Y.H.).

REFERENCES

- 1. Beinert H, Holm RH, Münck E. 1997. Iron-sulfur clusters: nature's modular, multipurpose structures. Science 277:653–659.
- 2. Lill R. 2009. Function and biogenesis of iron-sulphur proteins. Nature 460:831–838.
- 3. Burgess BK, Lowe DJ. 1996. Mechanism of molybdenum nitrogenase. Chem Rev 96:2983–3012.
- 4. Schilter D, Camara JM, Huynh MT, Hammes-Schiffer S, Rauchfuss TB. 2016. Hydrogenase enzymes and their synthetic models: the role of metal hydrides. Chem Rev 116:8693–8749.
- 5. Mühlenhoff U, Hoffmann B, Richter N, Rietzschel N, Spantgar F, Stehling O, Uzarska MA, Lill R. 2015. Compartmentalization of iron between mitochondria and the cytosol and its regulation. Eur J Cell Biol 94:292–308.
- 6. O'Brien E, Holt ME, Thompson MK, Salay LE, Ehlinger AC, Chazin WJ, Barton JK. 2017. The [4Fe4S] cluster of human DNA primase functions as a redox switch using DNA charge transport. Science 355: pii: eaag1789.
- 7. Mettert EL, Kiley PJ. 2015. Fe-S proteins that regulate gene expression. Biochim Biophys Acta 1853: 1284–1293.

- 8. Rees DC, Tezcan FA, Haynes CA, Walton MY, Andrade S, Einsle O, Howard JB. 2005. Structural basis of biological nitrogen fixation. Philos Trans A Math Phys Eng Sci 363:971–984.
- 9. Georgiadis MM, Komiya H, Chakrabarti P, Woo D, Kornuc JJ, Rees DC. 1992. Crystallographic structure of the nitrogenase iron protein from *Azotobacter vinelandii*. Science 257:1653–1659.
- 10. Rebelein JG, Stiebritz MT, Lee CC, Hu Y. 2017. Activation and reduction of carbon dioxide by nitrogenase iron proteins. Nat Chem Biol 13:147–149.
- 11. Watt GD, Reddy KRN. 1994. Formation of an all ferrous Fe₄S₄ cluster in the iron protein component of *Azotobacter vinelandii* nitrogenase. J Inorg Biochem 53:281–294.
- 12. Angove HC, Yoo SJ, Burgess BK, Münck E. 1997. Mössbauer and EPR evidence for an all-ferrous Fe₄S₄ cluster with S = 4 in the Fe protein of nitrogenase. J Am Chem Soc 119:8730–8731.
- 13. Musgrave KB, Angove HC, Burgess BK, Hedman B, Hodgson KO. 1998. All-ferrous titanium(III) citrate reduced Fe protein of nitrogenase: an XAS study of electronic and metrical structure. J Am Chem Soc 120:5325–5326.
- 14. Yoo SJ, Angove HC, Burgess BK, Hendrich MP, Münck E. 1999. Mössbauer and integerspin EPR studies and spin-coupling analysis of the [4Fe-4S]⁰ cluster of the Fe protein from *Azotobacter vinelandii* nitrogenase. J Am Chem Soc 121:2534–2545.
- 15. Yoo SJ, Angove HC, Burgess BK, Münck E, Peterson J. 1998. Magnetic circular dichroism study of the all-ferrous [4Fe-4S] cluster of the Fe-protein of *Azotobacter vinelandii* nitrogenase. J Am Chem Soc 120:9704–9705.
- 16. Stiebritz MT, Hiller CJ, Sickerman NS, Lee CC, Tanifuji K, Ohki Y, Hu Y. 2018. Ambient conversion of CO₂ to hydrocarbons by biogenic and synthetic [Fe₄S₄] clusters. Nat Catal 1:444–451.
- 17. Hiller CJ, Stiebritz MT, Lee CC, Liedtke J, Hu Y. 2017. Tuning electron flux through nitrogenase with methanogen iron protein homologues. Chemistry 23:16152–16156.
- 18. Strop P, Takahara PM, Chiu H, Angove HC, Burgess BK, Rees DC. 2001. Crystal structure of the all-ferrous [4Fe-4S]⁰ form of the nitrogenase iron protein from *Azotobacter vinelandii*. Biochemistry 40:651–656.
- 19. Schlessman JL, Woo D, Joshua-Tor L, Howard JB, Rees DC. 1998. Conformational variability in structures of the nitrogenase iron proteins from *Azotobacter vinelandii* and *Clostridium pasteurianum*. J Mol Biol 280:669–685.
- 20. Schindelin H, Kisker C, Schlessman JL, Howard JB, Rees DC. 1997. Structure of ADP x AIF₄-stabilized nitrogenase complex and its implications for signal transduction. Nature 387:370–376.

- 21. Jeoung JH, Fesseler J, Goetzl S, Dobbek H. 2014. Carbon monoxide. Toxic gas and fuel for anaerobes and aerobes: carbon monoxide dehydrogenases. Met Ions Life Sci 14:37–69.
- 22. Fesseler J, Jeoung JH, Dobbek H. 2015. How the [NiFe₄S₄] cluster of CO dehydrogenase activates CO₂ and NCO⁻. Angew Chem Int Ed Engl 54:8560–8564.
- 23. Kung Y, Drennan CL. 2011. A role for nickel-iron cofactors in biological carbon monoxide and carbon dioxide utilization. Curr Opin Chem Biol 15:276–283.
- 24. Can M, Armstrong FA, Ragsdale SW. 2014. Structure, function, and mechanism of the nickel metalloenzymes, CO dehydrogenase, and acetyl-CoA synthase. Chem Rev 114:4149–4174.
- 25. Nordlund S, Högbom M. 2013. ADP-ribosylation, a mechanism regulating nitrogenase activity. FEBS J 280:3484–3490.
- 26. Kazemi S, Safarifard V. 2018. Carbon dioxide capture in MOFs: the effect of ligand functionalization. Polyhedron 154:236–251.
- 27. Li D, Furukawa H, Deng H, Liu C, Yaghi OM, Eisenberg DS. 2014. Designed amyloid fibers as materials for selective carbon dioxide capture. Proc Natl Acad Sci U S A 111:191–196.
- 28. Sickerman NS, Hu Y, Ribbe MW. 2017. Nitrogenase assembly: strategies and procedures. Methods Enzymol 595:261–302.
- 29. Winn MD, Ballard CC, Cowtan KD, Dodson EJ, Emsley P, Evans PR, Keegan RM, Krissinel EB, Leslie AGW, McCoy A, McNicholas SJ, Murshudov GN, Pannu NS, Potterton EA, Powell HR, Read RJ, Vagin A, Wilson KS. 2011. Overview of the CCP4 suite and current developments. Acta Crystallogr D Biol Crystallogr 67:235–242.
- 30. Adams PD, Afonine PV, Bunkóczi G, Chen VB, Davis IW, Echols N, Headd JJ, Hung LW, Kapral GJ, Grosse-Kunstleve RW, McCoy AJ, Moriarty NW, Oeffner R, Read RJ, Richardson DC, Richardson JS, Terwilliger TC, Zwart PH. 2010. PHENIX: a comprehensive Python-based system for macromolecular structure solution. Acta Crystallogr D Biol Crystallogr 66:213–221.
- 31. Afonine PV, Grosse-Kunstleve RW, Echols N, Headd JJ, Moriarty NW, Mustyakimov M, Terwilliger TC, Urzhumtsev A, Zwart PH, Adams PD. 2012. Towards automated crystallographic structure refinement with phenix.refine. Acta Crystallogr D Biol Crystallogr 68:352–367.
- 32. Emsley P, Lohkamp B, Scott WG, Cowtan K. 2010. Features and development of Coot. Acta Crystallogr D Biol Crystallogr 66:486–501.
- 33. Davis IW, Leaver-Fay A, Chen VB, Block JN, Kapral GJ, Wang X, Murray LW, Arendall WB, Snoeyink J, Richardson JS, Richardson DC. 2007. MolProbity: all-atom contacts and structure validation for proteins and nucleic acids. Nucleic Acids Res 35:W375–W383.

- 34. The PyMol molecular graphics system, Version 2.0, Schrödinger, LLC.
- 35. Ahlrichs R, Bär M, Häser M, Horn H, Kölmel C. 1989. Electronic structure calculations on workstation computers: the program system turbomole. Chem Phys Lett 162:165–169.
- 36. O'Boyle NM, Banck M, James CA, Morley C, Vandermeersch T, Hutchison GR. 2011. Open Babel: an open chemical toolbox. J Cheminform 3:33.
- 37. Klamt A, Schürmann G. 1993. COSMO: a new approach to dielectric screening in solvents with explicit expressions for the screening energy and its gradient. J Chem Soc, Perkin Trans 2:799–805.
- 38. Tao J, Perdew JP, Staroverov VN, Scuseria GE. 2003. Climbing the density functional ladder: nonempirical meta-generalized gradient approximation designed for molecules and solids. Phys Rev Lett 91:146401.
- 39. Schäfer A, Huber C, Ahlrichs R. 1994. Fully optimized contracted Gaussian basis sets of triple zeta valence quality for atoms Li to Kr. J Chem Phys 100:5829–5835.
- 40. Weigend F, Ahlrichs R. 2005. Balanced basis sets of split valence, triple zeta valence and quadruple zeta valence quality for H to Rn: design and assessment of accuracy. Phys Chem Chem Phys 7:3297–3305.
- 41. Eichkorn K, Weigend F, Treutler O, Ahlrichs R. 1997. Auxiliary basis sets for main row atoms and transition metals and their use to approximate Coulomb potentials. Theor Chem Acc 97:119–124.
- Weigend F. 2006. Accurate Coulomb-fitting basis sets for H to Rn. Phys Chem Chem Phys 8:1057–1065.
- 43. Noodleman L. 1981. Valence bond description of antiferromagnetic coupling in transition metal dimers. J Chem Phys 74:5737–5743.
- 44. Noodleman L, Post D, Baerends E. 1982. Symmetry breaking and ionization from symmetry equivalent inner shells and lone pairs in Xα theory. Chem Phys 64:159–166.
- 45. Noodleman L, Peng CY, Case DA, Mouesca JM. 1995. Orbital interactions, electron delocalization and spin coupling in iron-sulfur clusters. Coord Chem 144:199–244.

FIGURES

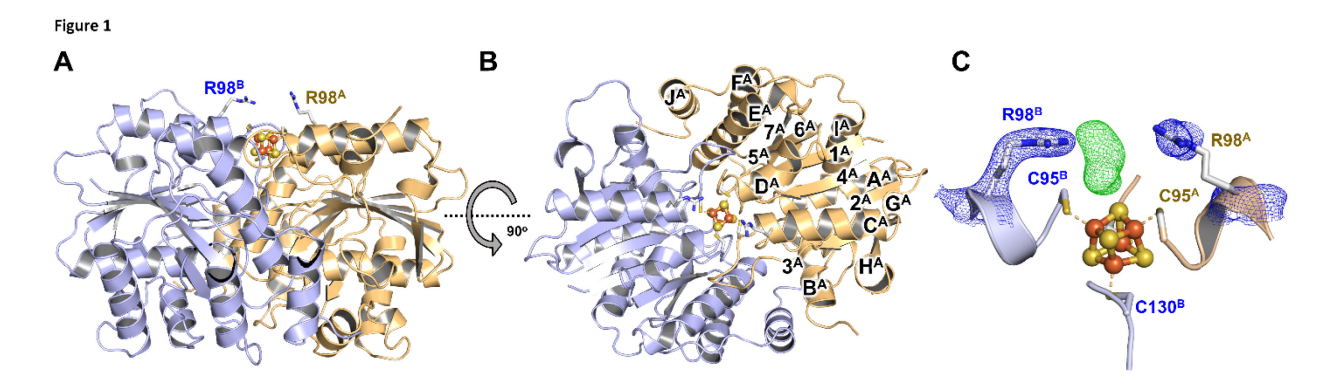


FIG 1 Side (A) and top (B) views of the 2.4 Å crystal structure of MaNifH. The subunits are shown as ribbons (subunit A, light orange; subunit B, light blue). The α-helices (A^A - J^A) and β-sheets (I^A - I^A) of subunit A are indicated. The [Fe₄S₄] cluster is shown in ball-and-stick presentation (Fe, orange; S, yellow). (C) The electron density (2Fo-Fc) of the active site of MaNifH was contoured at 1.5 σ level for the conserved Arg pair (blue meshes), and the omit map (Fo-Fc) of the additional electron density (green mesh) that is unaccounted for in the structure was contoured at 3.0 σ level. The four Cys ligands (C95^A, C130^A, C95^B, C130^B) and the conserved Arg pair (R98^A, R98^B) are shown as sticks.

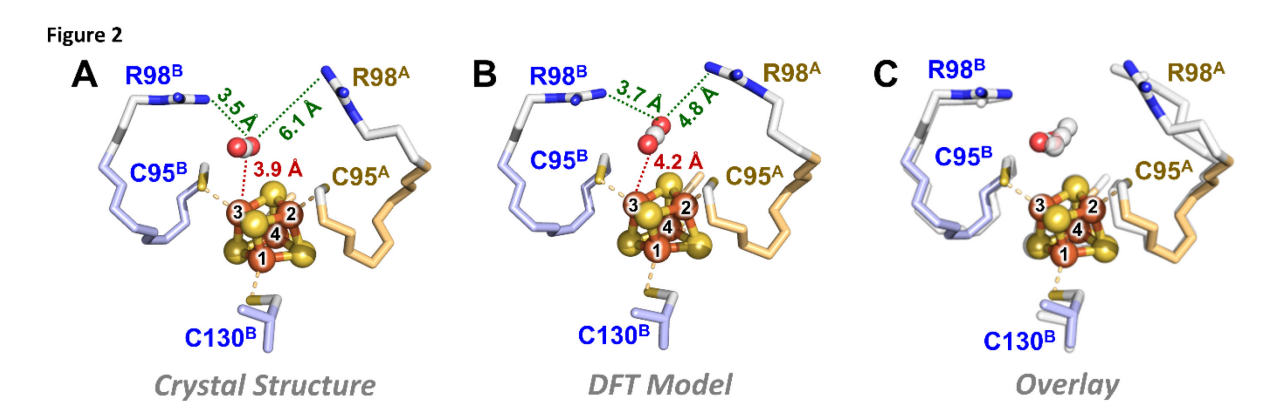


FIG 2 Crystal (A) and DFT-optimized (B) structures of *Ma*NifH with the extra electron density modeled as CO₂, and (C) an overlay of the two structures. The conserved pair of Arg residues assume 'proximal' (R98^B) and 'distal' (R98^A) positions, respectively, to the CO₂ moiety and the Fe3 atom of the cluster (A, B), and CO₂ occupies a highly similar position in the crystal structure and the DFT model (C). The [Fe₄S₄] cluster and CO₂ moiety are shown in ball-and-stick presentation and colored as follows: Fe, orange; S, yellow; C, gray; O, red. The Cys ligands and the conserved Arg residues are shown as sticks.

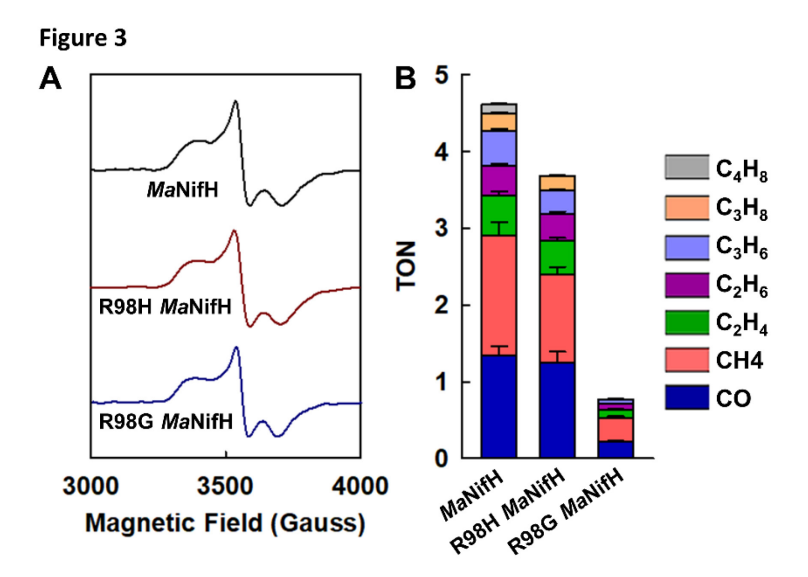


FIG 3 Spectroscopic and catalytic features of the wildtype and variant MaNifH. (A) EPR spectra and (B) CO₂-reducing activities of wildtype and variant MaNifH. EPR spectra were collected at 10 K. The wildtype, R98H and R98G MaNifH are dimers of ~60 kDa and contain 3.7 ± 0.1 , 3.9 ± 0.4 and 3.8 ± 0.2 nmol Fe per nmol protein, respectively. Like the wildtype MaNifH, the R98H and R98G variants display the same [Fe₄S₄]⁺-characteristic, S=1/2 EPR signal in the dithionite-reduced state (A); yet they display disparate activities in CO₂ reduction (B). The hydrocarbons/CO ratios (calculated based on total nmols of reduced carbons) of the wildtype MaNifH and R98H variant are 2.7 and 1.9, respectively, suggesting a shift from hydrocarbon-formation to CO-formation in the latter case.

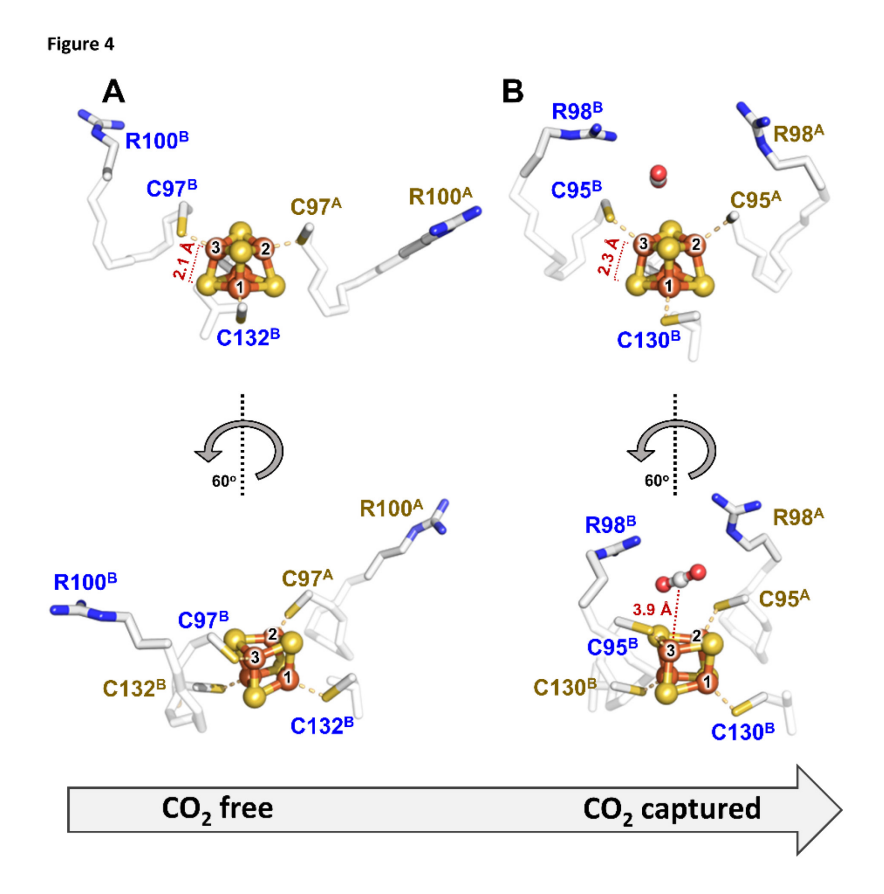


FIG 4 Comparison of the CO_2 -free (A) and CO_2 -captured (B) conformations of Fe protein, showing concerted yet asymmetric movement of a pair of conserved Arg residues that potentially capture CO_2 near the [Fe₄S₄] cluster. The CO_2 -free and CO_2 -captured conformations are represented by the homologous AvNifH and MaNifH, respectively. The movement of the 'proximal' Arg (R100^B in AvNifH and the corresponding R98^B in MaNifH) and the 'distal' Arg (R100^A in AvNifH and the corresponding R98^A in MaNifH) are shown from two angles.

SUPPORTING TABLE

Table S1. Data collection, refinement and ligand model statistics of MaNifH (PDB ID 6NZJ)

Space group	P6 ₅ 22		
Cell dimensions			
a, b, c (Å)	96.16, 96.16, 320.24		
α, β, γ (°)	90.00, 90.00, 120.00		
Wavelength (Å)	0.97741		
Number of reflections measured	419,306 (35,917)		
Number of unique reflections	35,959 (3,432)		
Resolution (Å)	$83.3 - 2.4 (2.5 - 2.4)^a$		
R _{meas} (%)	11.1 (78.1)		
$CC_{1/2}$	0.999 (0.810)		
Mean $I/\sigma(I)$	5.4 (1.0)		
Completeness (%)	100.0 (99.9)		
Multiplicity	11.9 (11.2)		
Resolution (Å)	83.3 - 2.4		
No. of reflections	35,369		
$R_{\text{work}}/R_{\text{free}}$ b (%)	18.31 / 21.80		
Number of atoms (non-H)			
Overall	4,147		
Protein	3,952		
Ligand	23		
Solvent	172		
Average B factors (A^2)			
Overall	49.01		
Protein	48.95		
Ligand	42.46		
Water	51.34		
Ramachandran plot statistics			
Favored (%)	96.49		
Allowed (%)	3.51		
R.M.S. deviations			
Bond lengths (Å)	0.008		
Bond angles (°)	0.90		
Statistics for the plausible ligands			

	Rwork (%) ^c	Rfree (%) ^c	Occupancy of the ligand ^d	Average B factor of the ligand (Å ²)	RSCC ^e
No ligand	18.31	21.80	-	-	-
CO_2	18.27	21.78	1.00	50.69	0.89
Glycerol	18.22	21.78	0.46	41.82	0.95
Carbonate	18.23	21.84	0.51	45.27	0.95

^aValues in parentheses represent the highest resolution shell.

TABLE S1. Date collection, refinement and ligand model statistics of MaNifH (PDB ID 6NZJ). Shown are the values for the ligand-free model (upper) and the statistics for the models with the plausible ligands CO₂, glycerol and carbonate (lower).

 $[^]bR_{work}$ was calculated using 95% of the data included in the refinement and R_{free} the 5% excluded data.

 $^{^{}c}R_{work}$ and R_{free} were calculated by Phenix.Refine. d The structure was refined by Phenix.Refine after the generation of each ligand.

^eReal-space correlation coefficient was provided by wwPDB Validation Server.

SUPPORTING FIGURES

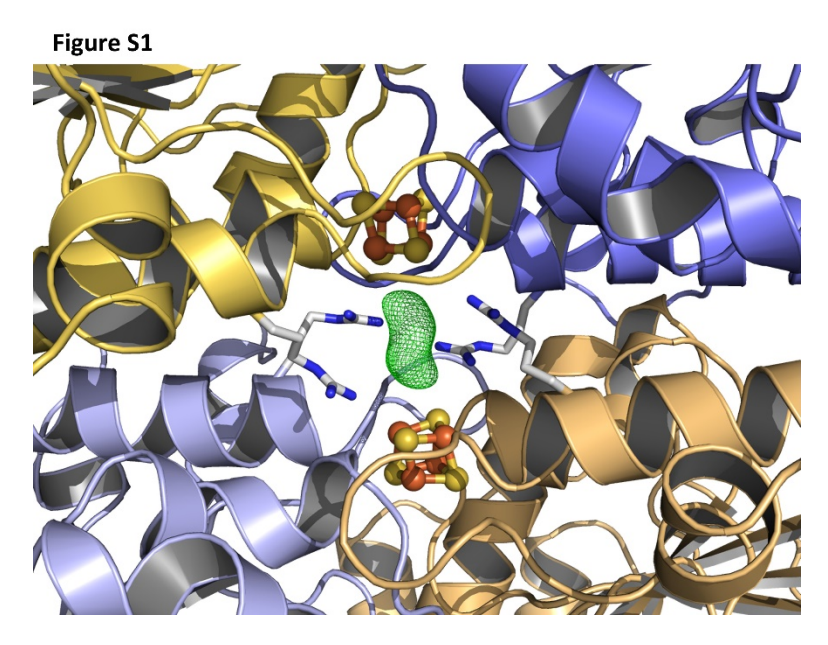


FIG S1 Structure of MaNifH without additional ligand. The subunits are shown as ribbons and colored light orange (subunit A) and light blue (subunit B) for the asymmetric unit, and yellow (subunit A) and dark blue (subunit B) for the symmetric mate. The Fo–Fc map (green mesh) is contoured at 3 σ . The side chains of R98 are shown as sticks. The [Fe₄S₄] clusters are shown in ball-and-stick presentation and colored as follows: Fe, orange; S, yellow.

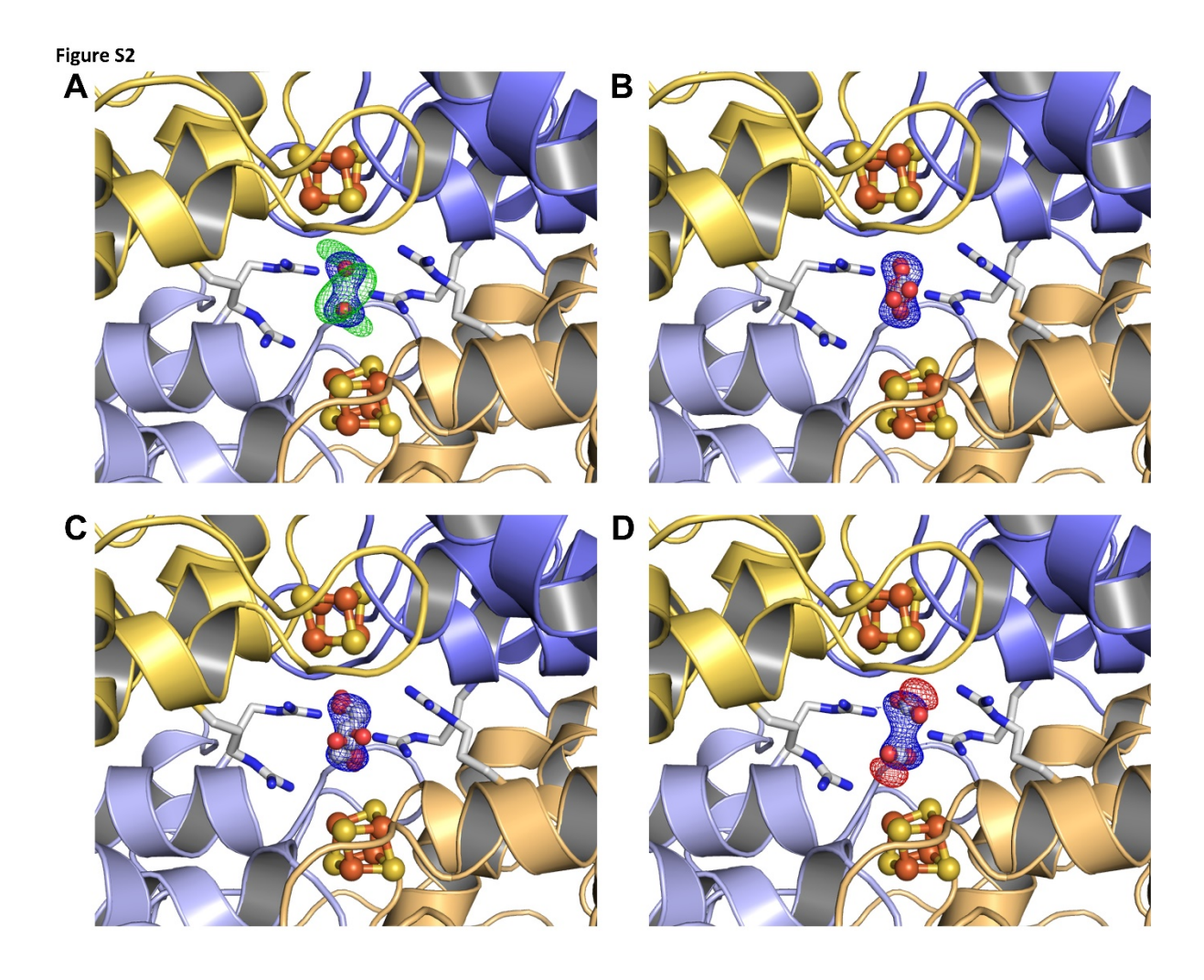


FIG S2 Structures of MaNifH modeled with two water molecules (**A**), two carbonate molecules (**B**), two glycerol molecules (**C**), and (**D**) two CO₂ moieties, respectively. The subunits are shown as ribbons and colored light orange (subunit A) and light blue (subunit B) for the asymmetric unit, and yellow (subunit A) and dark blue (subunit B) for the symmetric mate. The Fo–Fc map (red mesh) is contoured at -3 σ , the Fo–Fc map (green mesh) is contoured at 3 σ , and the 2Fo–Fc (blue mesh) map is contoured at 1.5 σ . One water (A) or CO₂ (B) molecule was modeled in the asymmetric unit and the other in the symmetry mate, respectively. The two carbonate (B) or glycerol (C) molecules were placed on the crystallographic axis. The side chains of R98 are shown as sticks. The [Fe₄S₄] cluster and the water, carbonate and glycerol moieties are shown in ball-and-stick presentation and colored as follows: Fe, orange; S, yellow; C, gray; O, red.

Figure S3

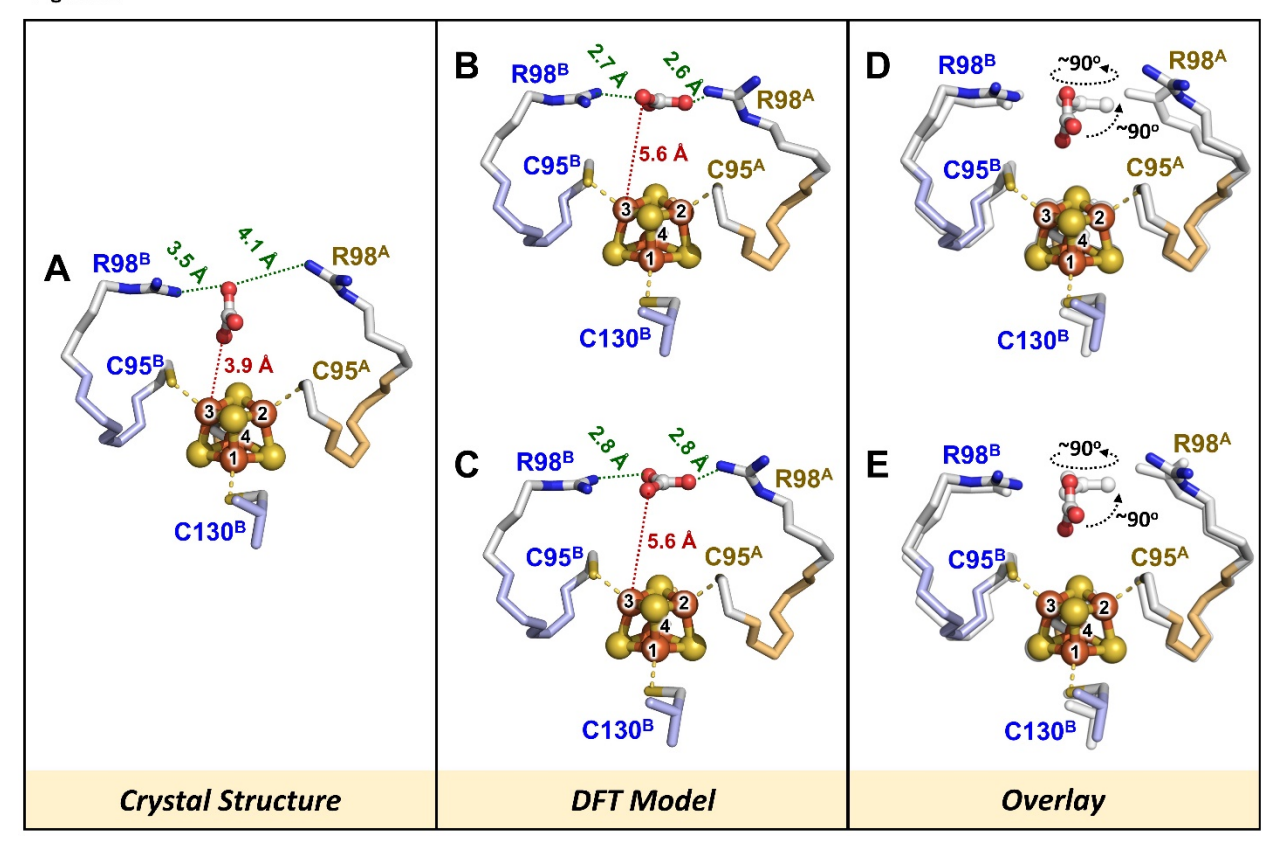


FIG S3 Crystal structure of MaNifH with the extra electron density modeled as carbonate (A) and DFToptimized structure of MaNifH with carbonate (B) or bicarbonate (C) as the substrate. In the crystal structure, the carbonate moiety assumes a position perpendicular to the upper surface of the [Fe₄S₄] cluster (A). Based on DFT-based structural optimization, however, carbonate is first protonated by R98^B and the resulting bicarbonate assumes a position parallel to the upper surface of the [Fe₄S₄] cluster (B). The DFToptimized structure calculated directly with bicarbonate (C) closely resembles that achieved with carbonate upon protonation (B). Overall, carbonate occupies a different position in the crystal structure than (bi)carbonate in the DFT models, which can be best visualized by the overlay of the carbonate-bound crystal structure with the (bi)carbonate-bound DFT models that originate either from the protonation of carbonate (D) or directly from bicarbonate (E). In both cases, the (bi)carbonate moiety swings ~90° from a position that is perpendicular to one that is parallel to the upper surface of the [Fe₄S₄] cluster. Furthermore, the (bi)carbonate moiety rotates ~90° counterclockwise in parallel to the upper surface of the cluster. The hydrogen atoms of bicarbonate are omitted from the figure, as they cannot be discerned by x-ray crystallography. The [Fe₄S₄] cluster and carbonate/bicarbonate moieties are shown in ball-and-stick presentations and colored as follows: Fe, orange; S, yellow; C, gray; O, red. The Cys ligands and the conserved Arg residues are shown as sticks.

Figure S4

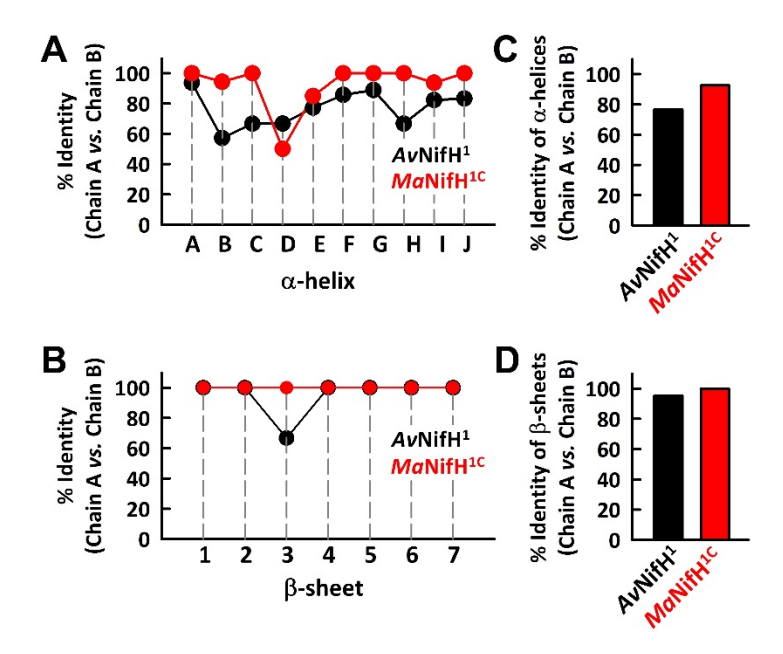


FIG S4 Identities between subunits A and B within AvNifH and MaNifH. Percentage identities between individual α-helices (**A**) and β-sheets (**B**) of subunits A and B within AvNifH (black) and MaNifH (red). Overall percentage identities between α-helices (**C**) and β-sheets (**D**) of subunits A and B within AvNifH (black) and MaNifH (red). Data from FIG S5 were used to calculate these percentages. Cα-deviations of subunit A vs. subunit B: AvNifH (0.356 Å) and MaNifH (0.334 Å).

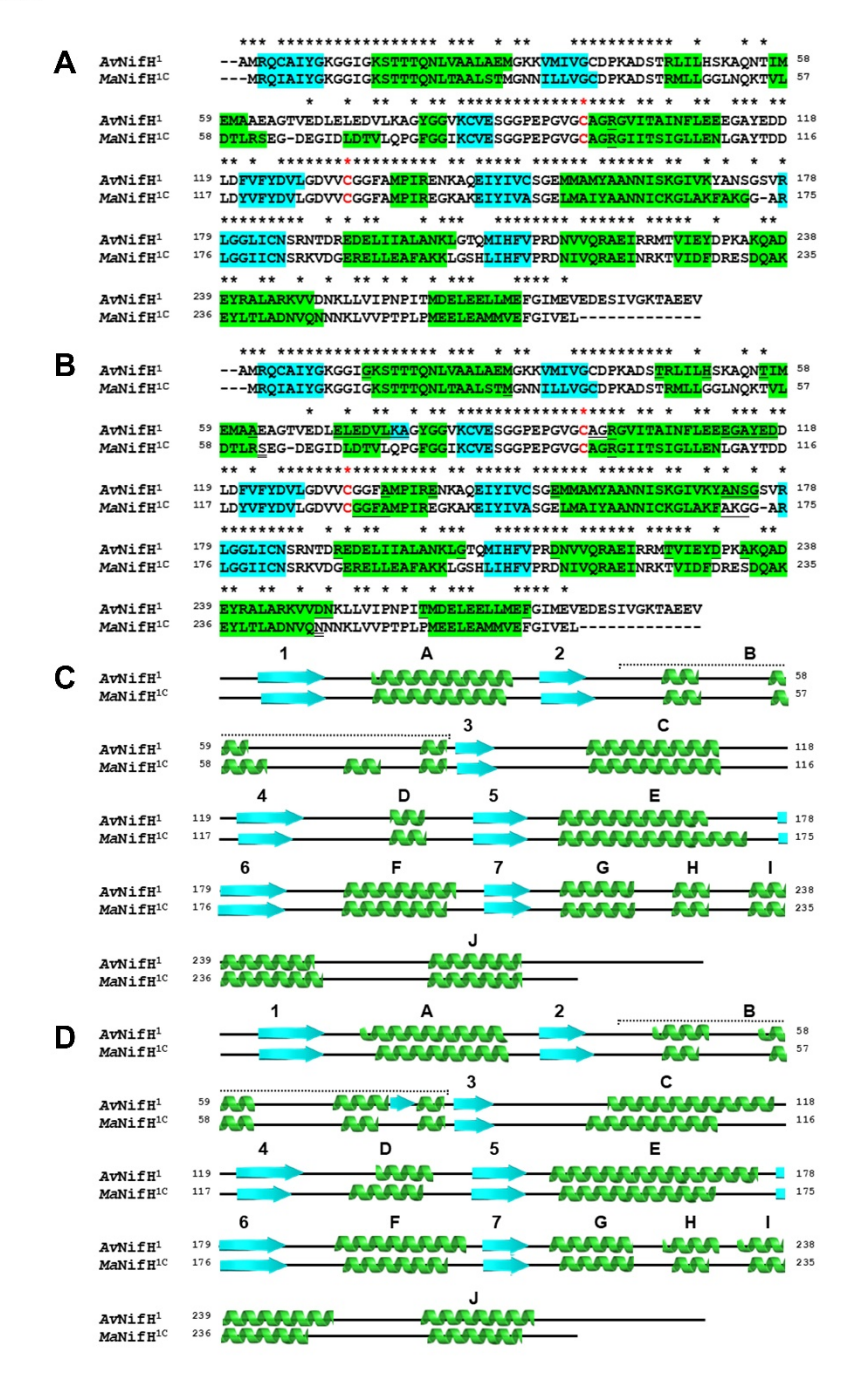


FIG S5 Subunits A and B of AvNifH and MaNifH. Comparisons between (A, B) primary sequences and (C, D) secondary structures of subunits A (A, C) and B (B, D) of AvNifH and MaNifH. The identical residues in the primary sequences are indicated with *, and the conserved Cys ligands for the [Fe₄S₄] cluster are shown in red (A, B). The α-helices are colored green, and the β-sheets are colored cyan (C, D); and the primary sequences corresponding to these structural elements are highlighted with the corresponding colors (A, B).

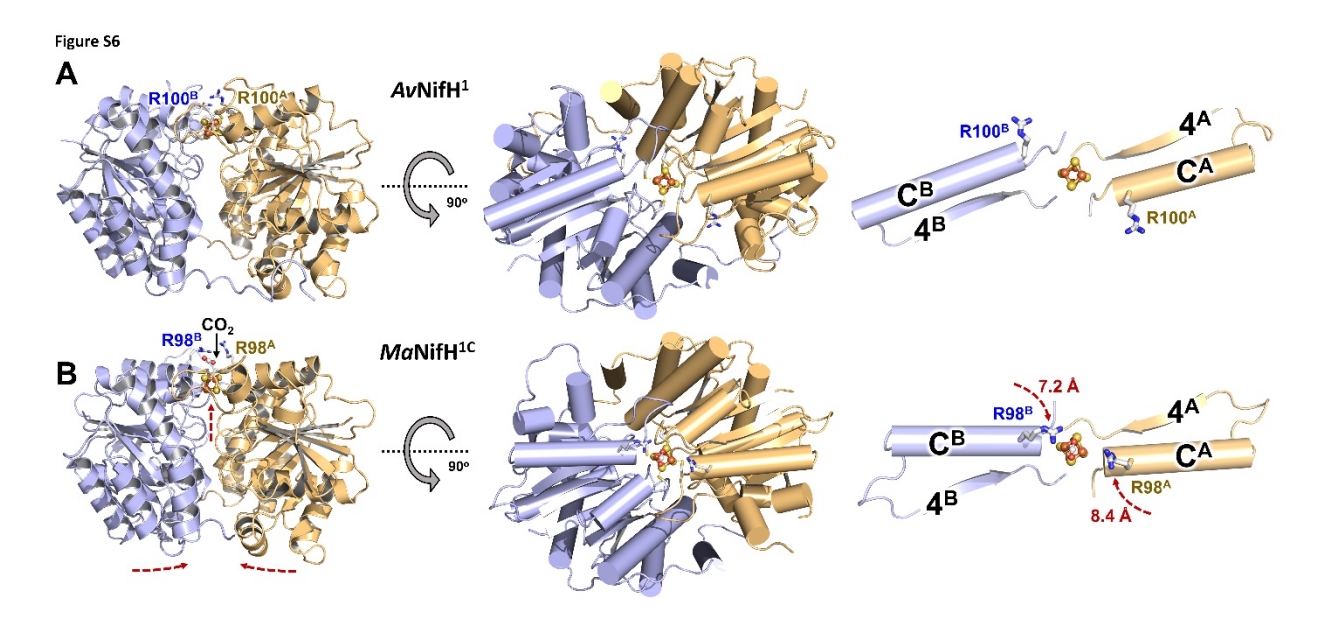


FIG S6 Structural comparison between AvNifH and MaNifH. Side (left) and top (middle) views of AvNifH (A) and MaNifH, with the alignments of helices C^B and C^A and the positions of the Arg pairs (located at the tips of helices C^B and C^A) highlighted (right). The movements of Arg residues in MaNifH (B, right) relative to those in AvNifH are indicated by dashed red arrows. Subunits are shown as ribbons (side view) or cylinders (top view) and colored light orange (subunit A) and light blue (subunit A), respectively. The [Fe₄S₄] cluster and CO₂ moiety are shown in ball-and-stick presentation and colored as follows: Fe, orange; S, yellow; C, gray; O, red.

SUPPORTING VIDEOS (Captions)

Video S1. Course of DFT-based structural optimization (TPSS/def2-SVP/def2-TZVP) of the CO₂-captured conformation of MaNifH in the [Fe₄S₄]¹⁺ state (S=1/2). The CO₂ moiety in the DFT-optimized structure is rendered gray, and the CO₂ moiety in the crystal structure is colored as follows: C, gray; O, red.

Video S2. Conformational morphing of AvNifH into MaNifH (side view). Both structures are depicted and colored as described in the legend of FIG S1. The conformational morphing plugin of PyMol 2.1.1 (https://pymol.org) was used to generate the movie, with AvNifH as the start conformation and MaNifH as the end conformation. Refinement cycles: 3; number of output states: 100; interpolation method: RigiMOL).

Video S3. Conformational morphing of AvNifH into MaNifH (top view). The movie was generated as described in the legend of Video S2.